J Solid State Electrochem (2009) 13:205–218
DOI 10.1007/s10008-008-0687-z

REVIEW

Site-specific adsorption of metallic and biological nanoparticles on nanostructured silicon surfaces

Katarzyna Skorupska

Received: 5 May 2008 / Revised: 13 August 2008 / Accepted: 20 September 2008 / Published online: 29 October 2008

Abstract The (photo)electrochemical preparation of nanostructures on single crystalline Si surfaces is described and surfaces are characterized by tapping mode atomic force microscopy (TM-AFM), Kelvin probe microscopy (KPM), high-resolution electron energy loss spectroscopy (HREELS), and synchrotron radiation photoelectron spectroscopy (SRPES). The H-terminated Si(111) surface and the step-bunched Si surface that exhibits multiatomic bilayer (BL) steps are prepared. HREELS demonstrates the low contamination levels achieved with the used *in-system* combined electrochemistry/surface analysis apparatus. With a miscut in the <1–21> direction, the surfaces prepared show a zigzag structure of the atomic terraces. These unique features provide the substrate for the (electro) deposition of platinum and for the immobilization of enzymes. Pt deposition, of relevance for the development of photovoltaic or fuel-generating solar cells, occurs predominantly at the edges of steps. On step-bunched surfaces, where KPM shows negative charging along the step edges and SRPES evidences the presence of an accumulation layer, the Pt nanoislands are considerably smaller than on H-terminated surfaces that are in flat band situation before deposition. SRPES analysis of the chemical and electronic condition after electrodeposition shows silicon oxide formation on both surfaces, suboxidic species, and the typical asymmetric Pt 4*f* core level lines. The results are discussed based on the details of the Pt deposition process at Si surfaces. As biomolecule, the enzyme reverse transcriptase (RT) of the avian myeloblastosis virus (AMV) was used. Immobilization is observed in TM-AFM experiments at the negatively charged step edges of the step-bunched surface. It is attributed to a superposition of attractive van der Waals and electrostatic interactions. The latter is related to the rather large Debye length of the carrier solution (~4 nm) and the overall positive charge of the RT where the pH of the carrier solution (pH 7) is smaller than that for the isoelectric point (IP) of 8.3.

Contribution to the Fall Meeting of the European Materials Research Society, Symposium D: 9th International Symposium on Electrochemical/Chemical Reactivity of Metastable Materials, Warsaw, 17–21 September 2007.

K. Skorupska (✉)
Division of Solar Energy, Interface Engineering Group,
Hahn-Meitner-Institut Berlin,
Glienicker Str. 100,
14 109 Berlin, Germany
e-mail: skorupska@hmi.de

Introduction

Metal electrodeposition and proteomics are presently of considerable interest in both fundamental and applied research. The former has found renewed interest due to the conformal attachment of metallic films also to rough substrates [1]; the feasibility to prepare, for instance by charge control, ultrathin, or discontinuous films [2]; and it is applied in the microelectronics industry [3] where Cu connects replace Al. In magnetoelectronics, electrodeposition is used for the fabrication of read heads [4] or for the investigation of exchange bias effects in ferromagnetic and antiferromagnetic film structures [5]. Electrodeposition is also used extensively in the fabrication of coatings for bioimplants [6] that are inert in physiological environment. In proteomics, large efforts are made on structural characterization that includes X-ray diffraction with variable photon energy as available at synchrotron sources [7]. For sensor technology, protein immobilization at solid surfaces is investigated and fundamental research relates to the understanding of structure–function relationships [8].

A common aspect in the two areas is the interaction of molecules and atoms with solid surfaces. In electrodeposition, it is well-known from experiments on highly ordered pyrolytic graphite (HOPG), for instance, that surface defects can act as nucleation sites [9]. Adsorption of biological molecules has been reported on metallic surfaces such as Au where surface functionalization was used for site-specific attachment [10] and on silicon oxide [11], for example. On semiconductors, metal deposition has been used to fabricate photovoltaic and photoelectrocatalytic devices [12, 13]. Protein or enzyme adsorption, however, has been mostly performed on metallic or insulating substrates [14, 15], although deposition onto semiconductors might be of interest for sensor applications [16]. On the molecular level, interaction of reactive gases such as O_2 and water vapor with semiconducting surfaces has been investigated to analyze the influence of the chemical nature of dangling bonds on adsorption and surface chemical changes [17]. For an improved understanding of the solid/adsorbate interaction in the actual deposition process and the subsequent physicochemical surface changes, the use of nanostructured surfaces with a high degree of order and specific surface chemical and electronic properties is highly desirable. Semiconductors allow to design specific electronic surface conditions ranging from flat band, depletion, inversion, and strong inversion to accumulation conditions [18]. Although electrostatic and structural effects could be superimposed, such surfaces might be of use for the realization of highly specific adsorbate–surface interactions.

In the present work, the step-bunched Si surface (SBSiS) is used as a nanostructured substrate [19]. It is characterized by large steps that are several bilayers (BL) high (5–15 BL) and by an accumulation condition [20, 21] as determined by synchrotron radiation photoelectron spectroscopy (SRPES). Locally resolved surface electronic characterization by Kelvin probe microscopy (KPM) and spatially integrated SRPES is employed to characterize this surface further. Subsequently, metal deposition and enzyme adsorption are investigated with respect to site specificity and, in the case of the reverse transcriptases (RTs), also with respect to nondestructive adsorption and imaging by atomic force microscopy (AFM).

Retroviruses RT was chosen for this experiment due to its unique structure and medical relevance. The RT plays a crucial role in the life cycle of retroviruses such as the human immunodeficiency virus I (HIV I) [22], which has been attracting considerable attention in the last three decades due to its relevance in acquired immunodeficiency syndrome. There are two activities that are characteristic for the RT: the synthesis of proviral DNA from viral RNA by a polymerase active side and the disintegration of viral RNA expressed by RNaseH activity. The avian myeloblastosis virus (AMV) RT that was used in the experiments described in this study contains two subunits of 65 and 105 kDa. Unfortunately, the X-ray three-dimensional structure of RT is available for the HIV I RT and not for AMV RT. The well-recognizable structure of HIV I RT is analogous with the human right hand [23, 24]. RTs of different retroviruses express the same activities. Due to this fact, the three-dimensional structure of all retrovirus' RTs resembles the right hand of a human [25–28]. Furthermore, the scanning tunneling microscope (STM) images for HIV I RT adsorbed on $MoTe_2$ surface [29] show similar biomolecule dimensions as were found in the AFM experiment for AMV RT.

Experimental methods and procedures

Materials

For the experiments, phosphorus-doped *n*-Si(111) with a resistivity of 6–12 Ωcm and 0° nominal miscut has been used. Ohmic contacts were made by a Ga–In eutectic on the previously scratched back side of the samples.

For surface preparation, very-large-scale integration quality 50% hydrofluoric acid (HF) and 40% ammonium fluoride (NH_4F) as well as acetone and ethanol reagents (Riedel-de Haën, Sigma-Aldrich Chemie, Taufkirchen, Germany) were used. Sodium hydroxide (NaOH) pellets with a purity of 99.998% (Aldrich) were employed.

The solution pH was adjusted by ultrapure H_2SO_4, HCl, or NaOH and controlled with a calibrated pH meter. For surface rinsing as well as solution preparation, MilliQ water (18 MΩcm specific resistivity) was applied. Solution purging and surface drying was done with 5 N N_2. Platinum electrodeposition was performed using hexachloroplatinic (VI) acid hexahydrate $H_2[PtCl_6]\cdot 6H_2O$ and potassium sulfate K_2SO_4 with 99.99% purity from Merck.

As biological samples, RTs of the AMV (Sigma) were investigated. The solution with the protein contains glycerol (50%), potassium phosphate (200 mM), dithiothreitol (2.0 mM), and Triton® X-100 (0.2%) (pH 7.2). The AMV RT was stored at −80 °C before use. Purification of biological samples was achieved using Pierce Dialysis Cassettes (3500 MWCO) with 0.1 to 0.5 mL capacity (Perbio Science, Thermo Fisher Scientific). For the dialysis, Tris base (Tris-hydroxymethyl-aminomethane) and ethylenediaminetetraacetic acid (EDTA) with 99.999% purity from the Sigma supplier have been used.

Methods

Electrochemistry was performed using an EG&G potentiostat 179, equipped with a coulometer in combination with an EG&G universal programmer 175 connected to an AD

converter and a computer for data recording. Experiments were done in the standard three-electrode potentiostatic arrangement with an Ag/AgCl reference electrode and a Pt counter electrode.

Two types of electrochemical surface preparations have been performed: (1) in ambient and (2) in N_2 atmosphere. For experiments in ambient air, a standard electrochemical cell was used. Sample preparation in N_2 avoids surface contamination and allows direct sample transfer from the electrochemical cell to a surface analysis machine. The specifically designed cell for combined *in-system* electrochemical and surface analytical measurements is shown in Fig. 1. It was used for SRPES, high-resolution electron energy loss spectroscopy (HREELS), and KPM. Figure 1 shows the glass vessel that is connected directly to the ultrahigh vacuum (UHV) chamber. The capillary with the Ag/AgCl reference electrode works also as an electrolyte supplier. Using N_2, the pressure created in the capillary forms an electrolyte drop below the Pt counter electrode. The electrical contact between the three electrodes and the drop of electrolyte is then formed by moving the sample holder with the silicon upwards. The electrochemical experiments were terminated by N_2 jet-blowing of the electrolyte drop, using a glass nozzle. Subsequently, the sample was rotated, rinsed with water (glass nozzle marked on a left side of Fig. 1), and then dried in N_2. The sample was then transferred into a buffer chamber for outgassing and, after the pressure reached values in the 10^{-9} Mbar range, transfer into the UHV analysis chamber was made.

SRPES has been performed using the Solid Liquid Analysis System (SoLiAS), connected to the U49/2 beam line at BessyII. Figure 2 presents a scheme of the SoliAS machine together with the connected electrochemical cell from Fig. 1. A silicon sample fixed to a Mo sample holder was introduced into the system at the load lock chamber. After stabilization of the pressure value (in the range of 10^{-5} Mbar), the sample was transported to a buffer chamber through the park and analysis chamber. Then, the sample was moved upwards to a park chamber and finally to the buffer chamber. From the buffer chamber, which was then filled with N_2, the sample was moved by a custom-made rod to the electrochemical cell. The pressure in the analysis chamber was in the 10^{-10} Mbar range.

Tapping mode atomic force microscopy (TM-AFM) imaging was made with a NanoScope III Scanning Probe Microscope (Digital Instruments, Santa Barbara, CA, USA) under ambient conditions. For imaging, silicon tips with a radius <10 nm were used. In case of biological samples, RTESP tips (Veeco) were employed. HREELS measurements were performed at the Fritz-Haber-Institut der Max-Planck-Gesellschaft. The glass vessel, shown in Fig. 1, was attached to the HREEL apparatus allowing for ultralow surface contamination even after electrochemical currents have been passed. The primary electron energy was 6 eV, the resolution was 11 meV. The pressure in the analysis chamber was in the range of 10^{-11} Mbar.

Surface preparation

Preparation of H-terminated silicon surface

For the measurement methods that are performed in UHV, the H-terminated silicon surface was prepared by an electrochemical procedure in the glass sphere–electrochemical cell (Fig. 1). The process was performed in three electrochemical steps. The procedure includes native oxide

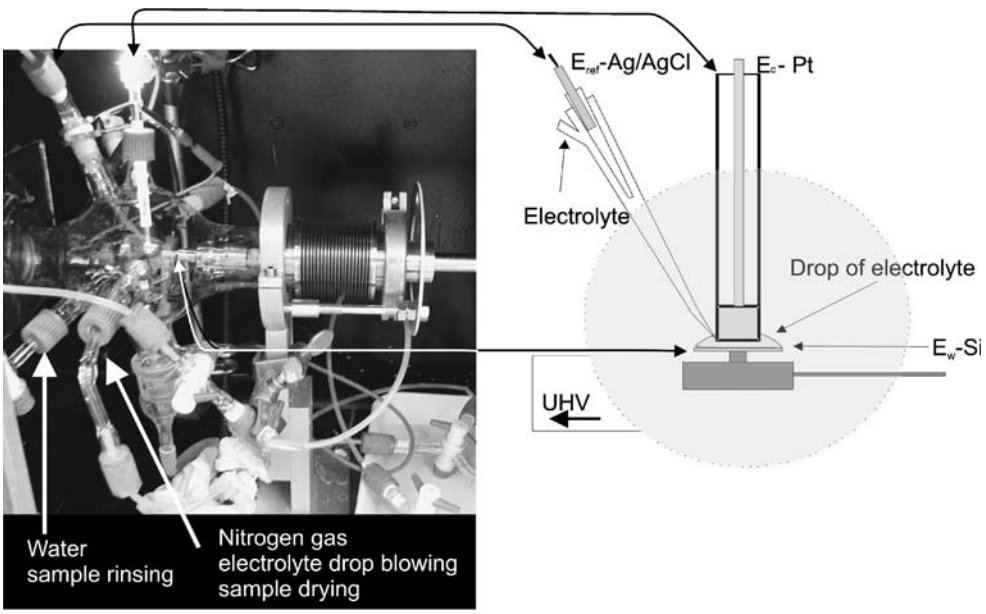

Fig. 1 Picture and scheme of the electrochemical cell for the sample preparation in nitrogen atmosphere. The glass vessel containing a transporting rod with the silicon sample fixed to a molybdenum holder and a three-electrode arrangement is connected directly to the UHV machine. In the drawing, the nozzles for nitrogen gas and water are not included to make the picture clearer. A system of the Teflon tubes and valves deliver the electrolytes to the capillary with the Ag/AgCl reference electrode. The glass rod with the platinum counter electrode can be also used for illumination of the silicon sample

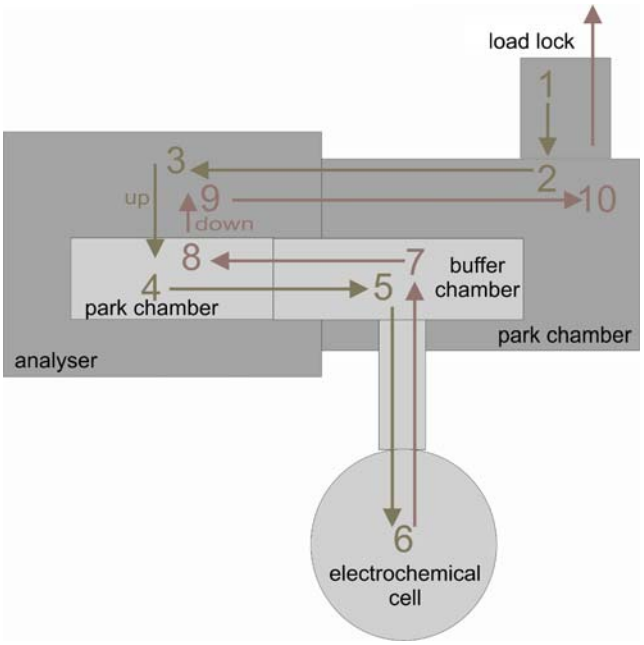

Fig. 2 Schematic drawing of the SoLiAS machine for SRPES measurements which is connected to the beam line U49/2 at Bessy in Berlin. The picture shows that the machine has two levels: the lower one with the load lock where the sample can enter the machine, the park chamber, and the chamber with the analyzer where measurements can be performed. The upper level contains the second park chamber and the buffer chamber. The vessel with the electrochemical cell is connected to the buffer chamber by a stainless steel UHV tube. In the buffer chamber, the outgassing of the sample after an electrochemical experiment takes place. With the *arrows*, the way of the sample in the machine is marked. With the *yellow arrows* (*1* to *6*), the way from the outside to the electrochemical cell is indicated. The *red arrows* mark the way from the electrochemical cell (*6*) to the chamber with the analyzer (*9*) where the measurement takes place and then to the exit

removal in dilute NH_4F solution of pH 4.0 by dark current etching at a potential of E=0.5 V vs. saturated calomel electrode (SCE). Then, a successive photooxidation in 0.1 M potassium hydrogen phthalate solution in a potential range from −0.5 to +9 V vs. SCE was conducted followed by further potentiostatic dark current etching in dilute NH_4F pH 4.0 and 4.9, respectively [30].

For measurements that were performed in ambient air, the H-terminated silicon surface was prepared by wet chemical etching that involved silicon dioxide removal in 50% hydrofluoric acid, an oxidation in H_2O_2–H_2SO_4 solution of 70 °C temperature, and etching in 40% ammonium fluoride solution.

Preparation of step-bunched silicon surface

The SBSiS on *n*-Si(111) was prepared in 2 M NaOH solution by cathodic polarization in the dark (Fig. 3). The potential was scanned from the open circuit potential (OCP) to a current density of about 100 μA with a scan rate of 5 mV/s. At 100 μA, the potential was held for 40 s.

Preparation of biological samples

The AMV RT was prepared by a dialysis against 10 mM Tris–HCl (Tris-hydroxymethyl-aminomethane) and 1 mM EDTA solution of pH 7.2 at a temperature of 6 °C. The mixture of 20 μL of the AMV RT with 250 μL of the buffer was placed in the dialysis cassette and immersed in a 2-L beaker filled with 1 L of the buffer solution. Stirring at a temperature of 6 °C for 24 h was applied; after this time, the buffer solution was changed and the system was stirred for another 24 h. The purified AMV RT was stored in an Eppendorf tube at 6 °C until a deposition experiment was performed.

Biomolecule deposition on SBSiS

The deposition was performed in ambient air at room temperature. Using an Eppendorf pipette, 10 μL of the dialyzed AMV RT was deposited on the SBSiS. The evaporation of the buffer solution under nitrogen sparge took about 30 min; after this time, the sample was ready for TM-AFM imaging.

Platinum electrodeposition

Platinum electrodeposition was conducted from 1 mM $H_2[PtCl_6]$ with 0.1 M K_2SO_4 solution of pH 3.5 in the dark at a potential of −0.8 V vs. SCE where deposition is

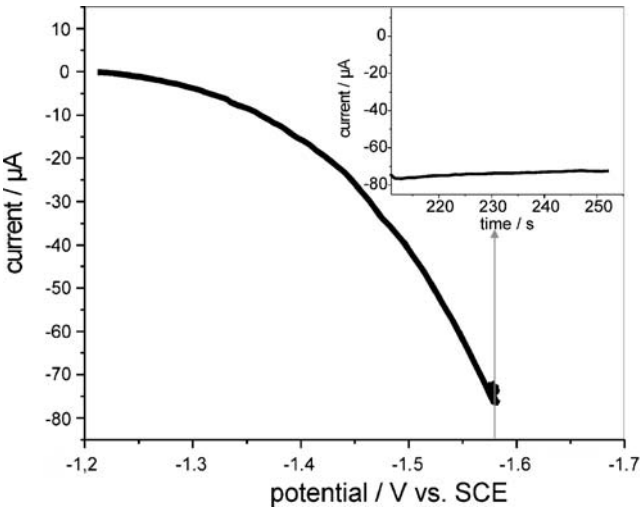

Fig. 3 Current vs. potential curve for *n*-Si(111) in 2 M NaOH solution. The measurement was performed in the dark. The sample's area was 0.8 cm^2. The potential was scanned from the open circuit value until the current density reached about 100 μA and then held for 40 s. The *inset* shows the current vs. time curve for the held potential value of −1.58 V vs. SCE

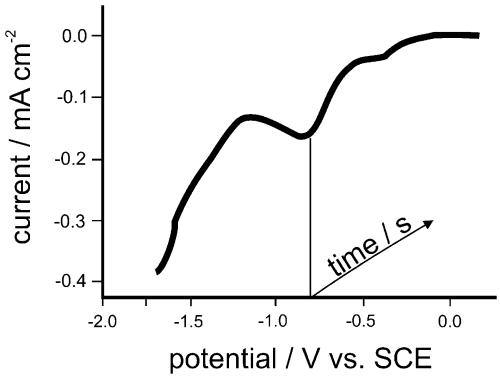

Fig. 4 Current density vs. potential curve for H-terminated *n*-Si(111) in 1 mM $H_2[PtCl_6]$ with 0.1 M K_2SO_4 solution of pH 3.5. There are two peaks visible at −0.38 and −0.8 V vs. SCE

expected. Figure 4 shows a typical current vs. potential curve for the above-mentioned condition where OCP is equal to +0.38 V vs. SCE.

Results and discussion

Topographical and spectroscopical characterization of substrates

H:Si(111) (1× 1)surfaces

Figure 5 presents a TM-AFM image of a H-terminated Si (111) surface prepared by wet chemical etching. Atomically flat terraces with a zigzag structure of about 100 nm width and 1 BL height (3.14 Å) can be seen.

The quality of the electrochemical preparation of H-terminated silicon surfaces is reflected by HREELS measurements (Fig. 6). The spectrum shows losses at 79 meV (Si–H bending mode), 258 meV (Si–H stretching mode), and a very small signal at 113 meV (Si–H–H scissor

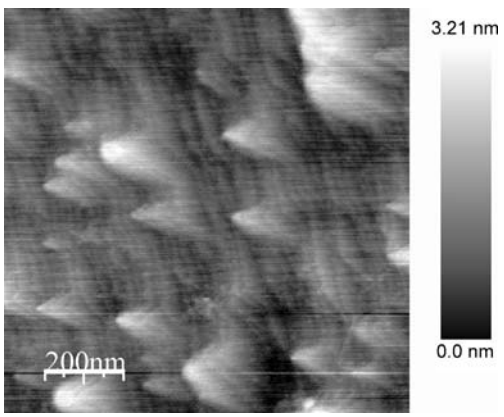

Fig. 5 TM-AFM picture of a chemically H-terminated *n*-Si(111) surface

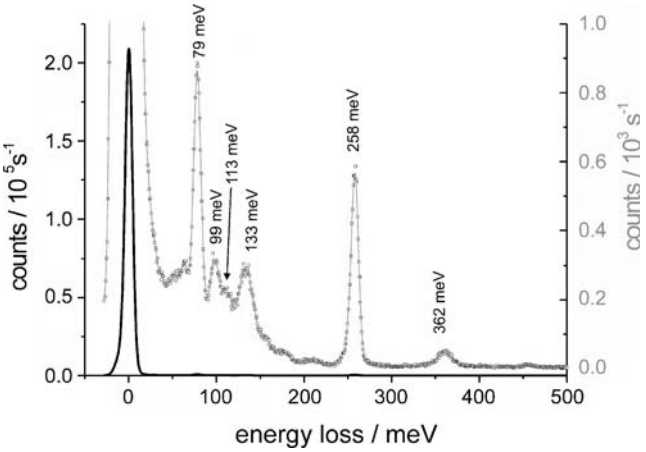

Fig. 6 HREEL spectrum for H-terminated *n*-Si(111) prepared by the electrochemical procedure

mode). These losses were also found on the chemically prepared H:Si(111) surface [31]. The spectrum in Fig. 6 presents also losses at 99 meV (Si–OH bending mode or/ and Si–F stretching mode) and at 133 meV (bridge-bonded O). Additionally, a small peak at 362 meV (C–H stretching mode) is observed.

Figure 7 shows the SRPES data for a chemically prepared *n*-type H:Si(111) surface. The Si 2*p* line has been recorded for an excitation energy of 150 eV which corresponds with the escape depth λ_{esc}=4 Å. The characteristic position for *n*-Si at 99.8 eV with no signal at higher bonding energy, which would be an indication for the presence of silicon dioxide, can be observed.

The valence band onset at 0.85 eV vs. the Fermi level (E_F) for a photon energy of 150 eV is presented in Fig. 8. The distance between the valence band edge and E_F indicates that H:Si(111) (1×1) is in flat band situation as the measured energetic distance correlates exactly with the difference $E_F - E_{VB}$, given by the doping concentration.

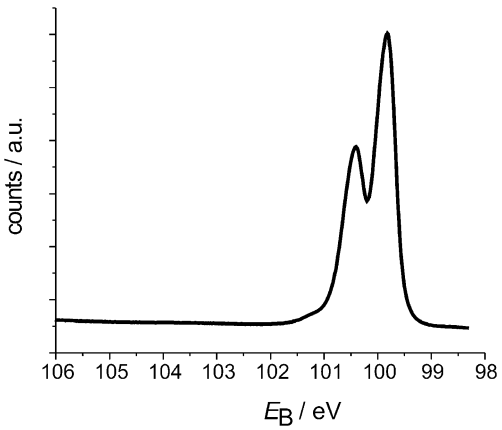

Fig. 7 SRPE spectrum for an excitation energy of 150 eV presenting the Si 2*p* line for the electrochemically H-terminated *n*-Si(111) surface

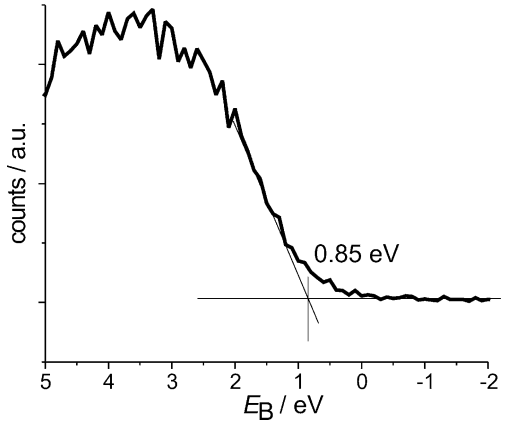

Fig. 8 SRPE spectrum for the excitation energy of 150 eV presenting the valence band onset at a value of 0.85 eV for the electrochemically H-terminated *n*-Si(111) surface

The H-terminated Si surface constructed by atomically flat terraces in flat band condition has been used a "standard" surface for platinum electrodeposition experiments. For conceptional reasons, this surface was not considered as particularly useful for biomolecule adsorption experiments.

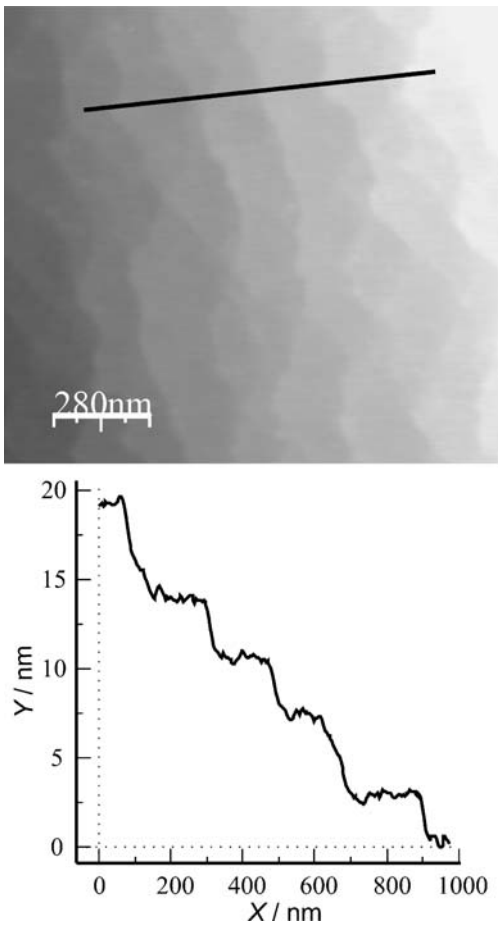

Fig. 9 TM-AFM image and its cross section of the SBSiS

The step-bunched Si(111) surface

A TM-AFM image and a cross section of the SBSiS is shown in Fig. 9. The steps range from about 4.5 to 5 nm in height and from 100 to 200 nm in width, mainly leveling 150 nm. A closer inspection of the steps height gives values of *x*•BL where *x* is the number of atomic BL, one atomic bilayer is 3.14 Å high. The angles between steps, which are constructed by (111) crystallographic planes, and step sides reveal values of about 60°. The crystallographic plane of the step walls could be attributed to the (100) surface which forms an angle of 54.7° with the (111) surface. The presence of (100) surfaces at the step edges of SBSiS is in good agreement with SRPES data [20, 21] which show the presence of silicon bonded with two hydrogen atoms (Si–H–H) and silicon bonded with one hydrogen atom and one hydroxyl group (Si–H–OH). The presence of –OH groups at the silicon surface makes the surface of step edges more hydrophilic due to larger electronegativity difference.

The SRPES spectrum (Fig. 10) of the SBSiS for excitation energies of 150 and 585 eV, respectively, shows the original data (as were obtained) in the upper part of the picture as well as the deconvoluted silicon bulk signals

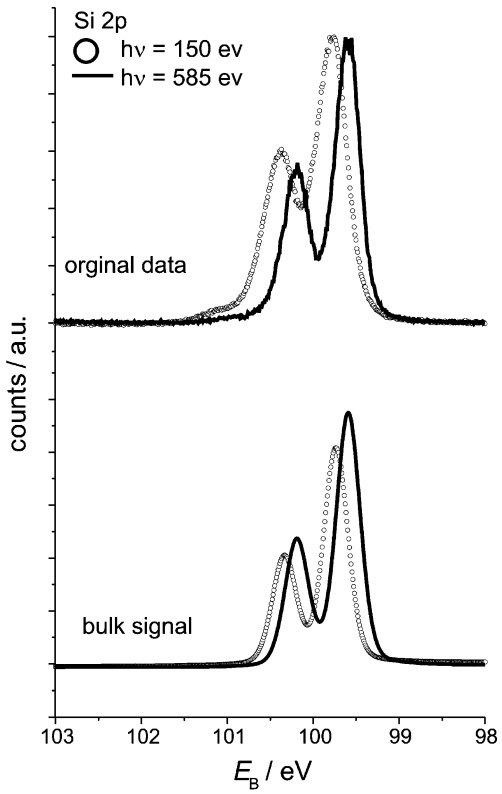

Fig. 10 SRPES data for the SBSiS. The *upper* part contains the Si 2*p* lines original data, the *lower* part shows the bulk signals. In both cases, there are spectra for excitation energies of 150 eV (*circles*) and 585 eV (*line*)

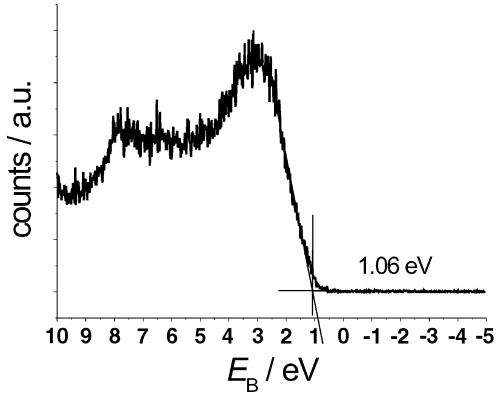

Fig. 11 The valence band onset SRPES data for the SBSiS. The excitation energy equals 150 eV

beneath them. It is clearly visible that with increasing excitation energy, the spectra are shifted in the direction of lower binding energy, amounting to 0.2 eV. Figure 11 shows the valence band onset at 1.06 eV. The distance of 1.06 eV between valence band and Fermi level indicates an accumulation situation in the space charge region with a negative band bending of 0.2 eV. The results for the KPM presented in this study in form of a simple diagram (Fig. 12) show a contact potential drop at the step edges [32]. The potential decrease in the region near step edges suggests a spatially inhomogeneous distribution of the accumulation situation on the surface. These properties make the SBSiS an interesting substrate for adsorption studies.

Platinum deposition on H:Si(111) (1×1) and step-bunched Si(111) surfaces

Platinum electrodeposition was performed on both H-terminated and SBSiS. The comparison of results obtained on H-terminated Si surface used reference surface with those on SBSiS provides information about the influence of SBSiS on the deposition process.

The TM-AFM image in Fig. 13 shows the surface nanotopography of an H-terminated silicon surface after platinum electrodeposition. One can see two kinds of platinum islands on the surface. While the smaller ones are about 5 nm in height and less than 100 nm wide, the larger ones present a height of approximately 30 nm and a

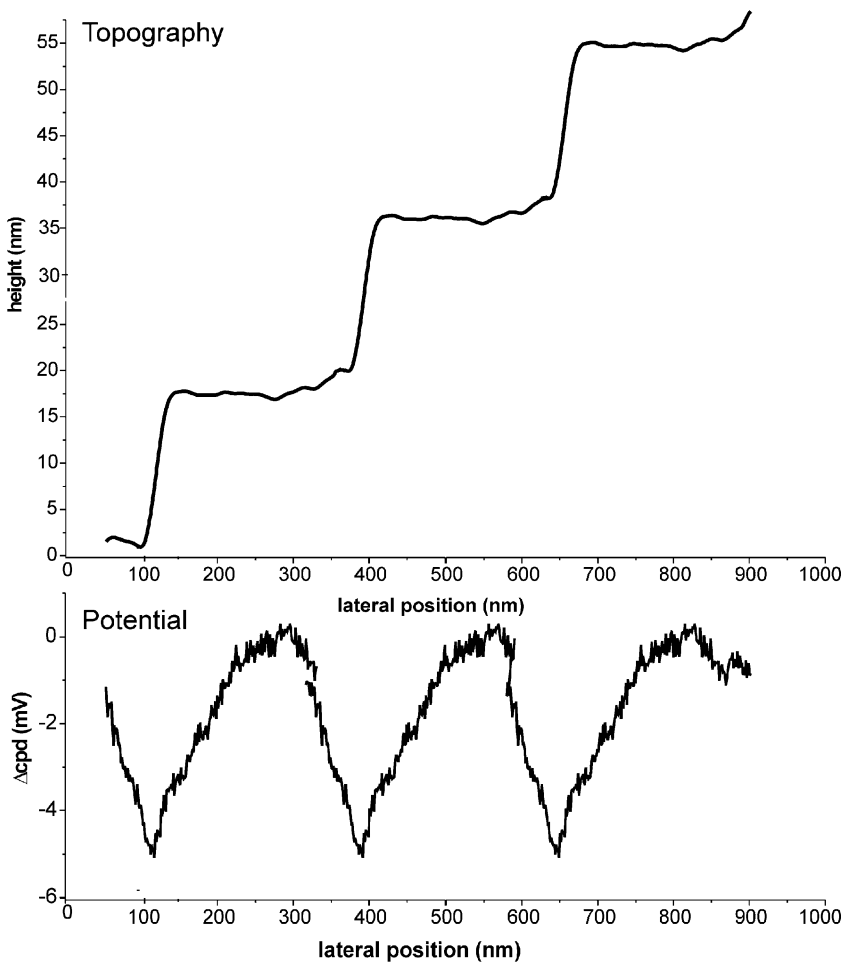

Fig. 12 The diagram for KPM results on the SBSiS

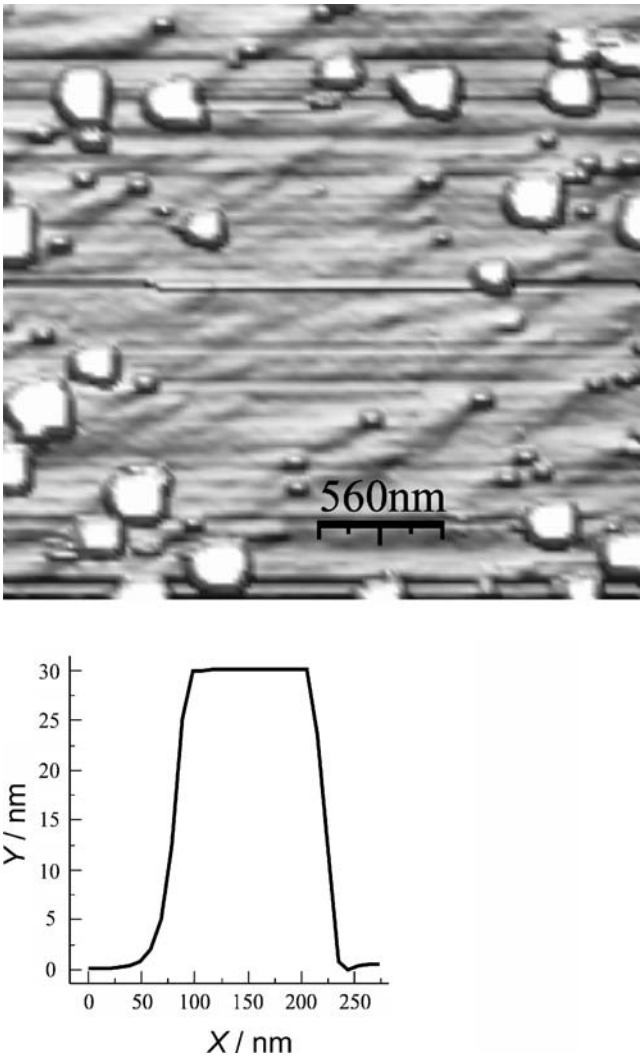

Fig. 13 TM-AFM image with cross section for the H-terminated silicon surface after platinum electrodeposition

width of 150 to 200 nm. Figure 14 shows a TM-AFM image after platinum deposition on the SBSiS. In this case, the platinum islands are roughly 3 nm high and 40 to 80 nm wide. The position of Pt dots at the step edges can be seen in the cross sections of Fig. 14. On the H-terminated surface (Fig. 13), due to the size ratio between the dots and the terraces, the localization of the metal particles is not as clear as for the SBSiS where the steps are much higher (Fig. 14). Nevertheless, the metal dots seem to be localized mainly at step edges.

The SRPES data with the Si 2*p* lines for the H-terminated and the SBSiS (Fig. 15a,b) show the presence of SiO_2 that is indicated by the emission shifted by 4 eV from the Si 2*p* peak. The ratio between the two peaks indicates that a larger amount of silicon dioxide is produced during platinum electrodeposition on the H-terminated silicon surface.

The presence of silicon dioxide is also confirmed by the O 1*s* lines for the two surfaces. Figure 16 shows the normalized signals for O 1*s* where contributions for 532, 533, and 534 eV are indicated. The signal for 533 eV is attributed to silicon dioxide whereas the signals for 532 and 534 eV are attributed to hydroxides and molecular water, respectively. It is difficult to predict whether silicon oxide creates a close film on the surface or an island type structure. Additionally, the presence of an ultrathin, conductive silicon dioxide layer between the platinum islands and the silicon substrate cannot be excluded.

Using Eq. 1 and the Si 2*p* spectra from Fig. 15, the thickness of silicon dioxide can be calculated [33, 34]. Thus, oxide thicknesses of 3.5 and 2.5 Å were calculated for the H-terminated and the SBSiS, respectively:

$$d = \lambda_f \times \ln\left(\frac{I_{ox}}{I_{Si}} \times \frac{I_{Si}^{\infty}}{I_{ox}^{\infty}} + 1\right) \quad (1)$$

where λ_f is the mean inelastic length of photoexcited electrons with kinetic energy E, I_{film}^{∞} and $I_{substrate}^{\infty}$ are the intensities of pure elements, $I_{film}^{SiO_2}$ and $I_{substrate}^{Si}$ are the measured line intensities, and d is the overlayer thickness.

The Pt 4*f* signals for H-terminated and SBSiS in Fig. 17 present the typical position for metallic platinum at 71.2 eV. The observed asymmetry of the 4*f* core level can be attributed to the interaction of the core hole created in the photoelectron excitation process with less mobile electrons from the *d*-orbital at the Pt Fermi level [35].

During the cathodic polarization of the silicon electrode in the platinum-containing solution, the following three processes can take place: platinum deposition, silicon oxide formation, and H_2 evolution. The possibility of Pt oxide formation can be excluded, since the signals for oxidized Pt expected at E_B=530.3 eV for PtO and at 530.5 eV for PtO_2 were not found in the O 1*s* line (Fig. 16). The formation of silicide [36] can also be excluded due to the high temperature treatment (>200 °C) that would be needed to the development of Pt_2Si and finally PtSi at the interface.

The platinum electrodeposition can be described by reactions 2, 3, and 4 that are also observed for the HOPG substrate [37]:

$$PtCl_6^{2-} + 2e^- \rightarrow PtCl_4^{2-} + 2Cl^- \quad (V = 0.708\,\text{V vs. SCE}) \quad (2)$$

$$PtCl_4^{2-} + 2e^- \rightarrow Pt + 4Cl^- \quad (V = 0.535\,\text{V vs. SCE}) \quad (3)$$

$$PtCl_6^{2-} + 4e^- \rightarrow Pt + 6Cl^- \quad (4)$$

The nature of interactions between the negatively charged electrode surface and the $PtCl_6^{-2}$ as well as $PtCl_4^{-2}$

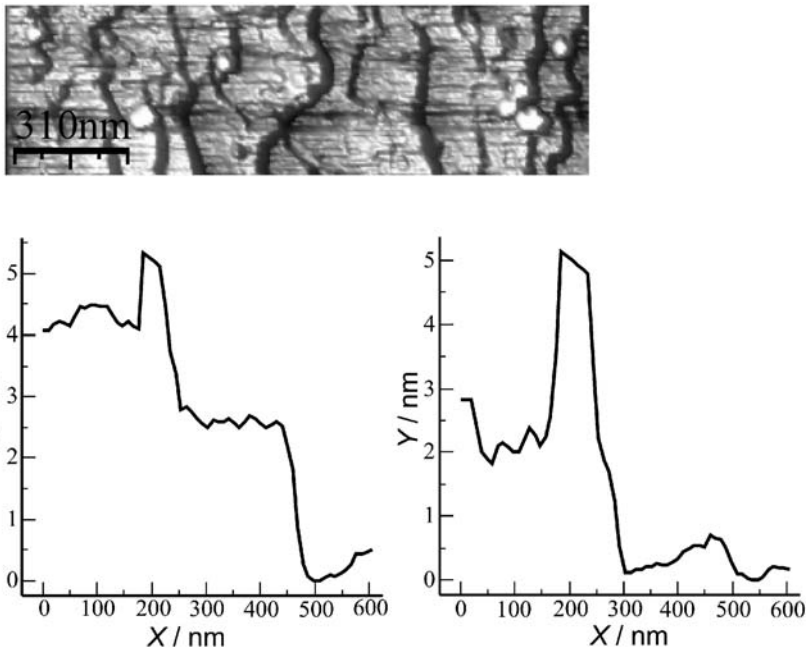

Fig. 14 TM-AFM image with cross sections for the SBSiS after platinum electrodeposition

ions are not fully understood and some models were discussed [38]. It is difficult to explain the platinum deposition process by a simple outer sphere electron reaction as the hexachloroplatinum and tetrachloroplatinum complexes are expected to be localized in the diffuse layer in the outmost part of the electrical double layer. Specifically adsorbed molecules in the inner Helmholtz layer (IHL) are partially solvated, while solvated cations such as H^+ and K^+ are located in the outer Helmholtz layer (OHL). The position of the $PtCl_6^{-2}$ and $PtCl_4^{-2}$ ions, if they are not specifically adsorbed, would be in the diffuse layer. In this

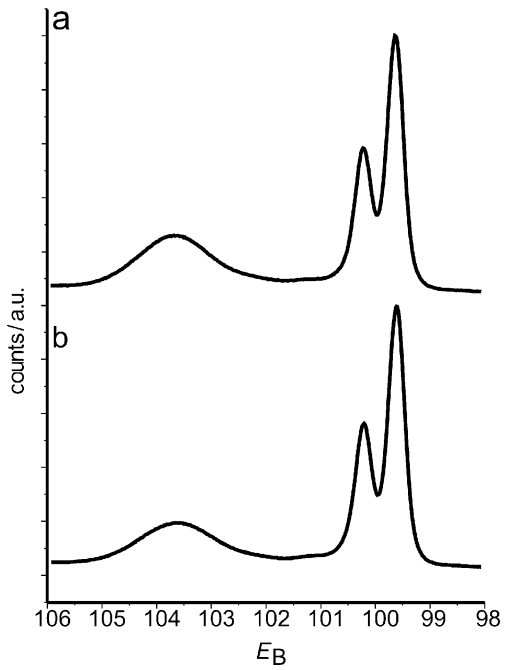

Fig. 15 SRPES data, Si 2*p* lines for *a* H-terminated *n*-Si(111) after platinum electrodeposition and *b* a SBSiS after platinum electrodeposition

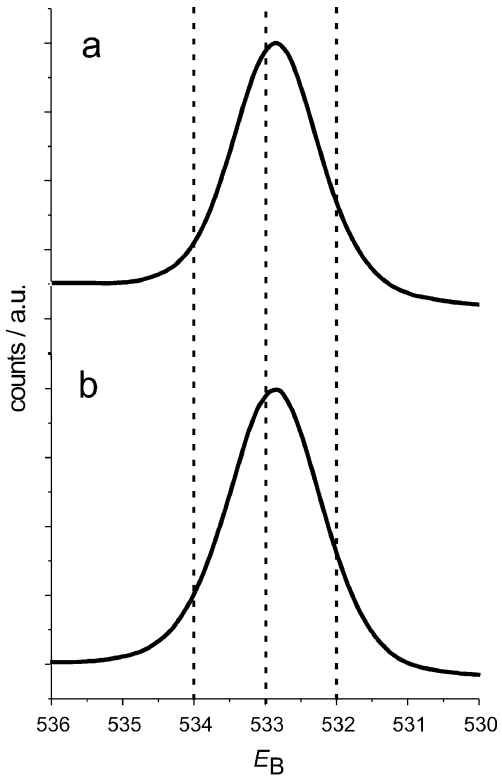

Fig. 16 SRPES data, O 1*s* lines for *a* H-terminated *n*-Si(111) after platinum electrodeposition and *b* a SBSiS after platinum electrodeposition

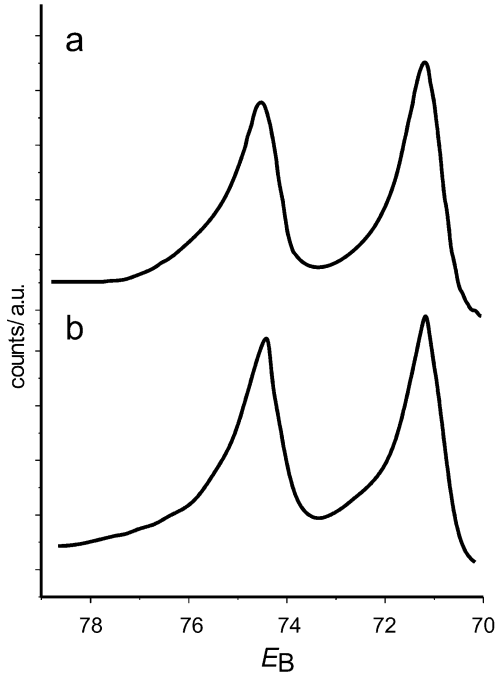

Fig. 17 SRPES data, Pt 4*f* lines for *a* H-terminated *n*-Si(111) sample after platinum electrodeposition and *b* SBSiS after platinum electrodeposition

case, the electron transfer would proceed by an outer sphere charge transfer mechanism [39]. The specific adsorption of the chloroplatinic anions seems to be more likely. The adsorption of metal complexes at electrode surfaces as gold cyanide adlayers on gold electrode [40] and silicotungstate adlayers on a silver electrode [41], for instance, is well-known. The adsorption of the hexachloroplatinate complex on gold and platinum surfaces during platinum electrodeposition was investigated by Uosaki et al. [42, 43]. These authors assumed a 2D model of an adsorbed $PtCl_6^{-2}$ layer to explain obtained STM images. According to this model, $PtCl_6^{-2}$ ions are adsorbed through three of their six coordination chloride atoms. The adsorbed layer disappeared after the electrode was rinsed with a $PtCl_6^{-2}$-free solution, indicating a weak adsorption of the platinum complex. Lau and Hubbard [44, 45] studied the reduction mechanism of Pt(IV) and Pt(II) complexes. The inhibiting effect of specifically adsorbed chloride atoms in the electroreduction of $PtCl_4^{-2}$ and, to a lesser extent, of $PtCl_6^{-2}$ has been outlined. The authors reported that the adsorption of the planar $PtCl_4^{-2}$ ion requires more free adsorption sites at the electrode surface in comparison with octahedral $PtCl_6^{-2}$. For this reason, the increase of the Cl^- concentration in the electrolyte hindered the reduction of Pt (II) to a larger extent than the reduction of Pt(IV).

Possible interaction forces between chloroplatinum complexes and silicon surface seems to be of van der Waals type. But at this state of knowledge, it is difficulty to make final conclusions. The formation of hydrogen bridge bonds (~0.4 eV) between –OH groups bonded to silicon surface atoms and chlorometallate complexes seems to be probable. Hydrogen bridge bonds with Si–H···X can be excluded due to the small electronegativity of silicon atoms.

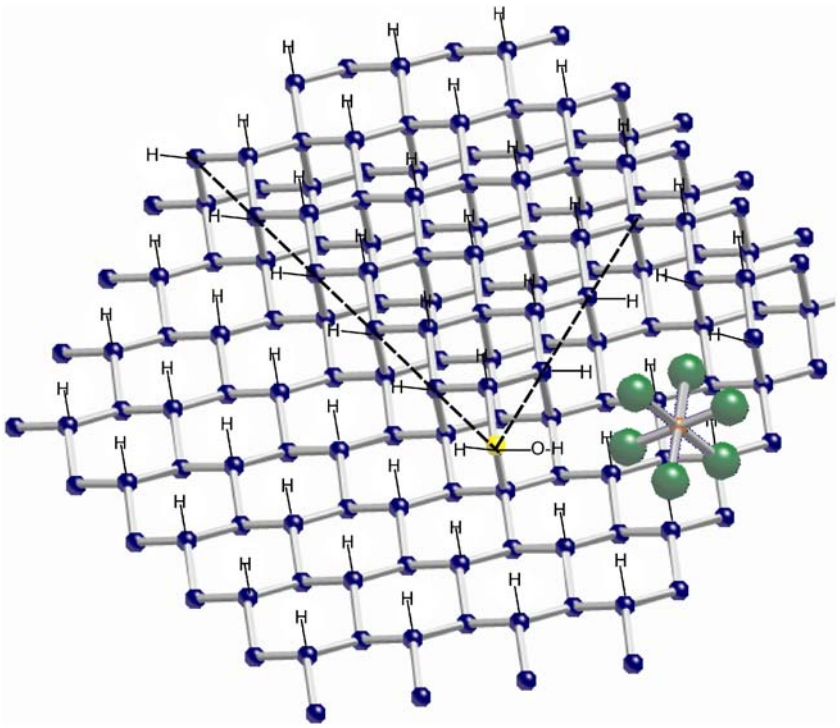

Fig. 18 Stick boll model of Si (111) surface with terrace and kink side atom (*yellow boll*) and adsorbed $PtCl_6^{-2}$ ion

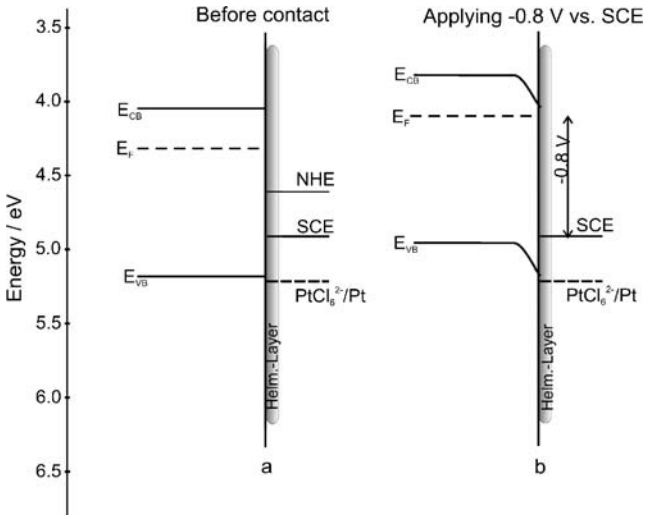

Fig. 19 Energy band diagram showing *a* the energy band alignment for *n*-Si and solution used for platinum electrodeposition and *b* the energetical situation for *n*-Si immersed in the platinum electrodeposition solution when the potential of −0.8 V vs. SCE is applied

Looking at the AFM images (Figs. 13 and 14), it is seen that deposits are localized at step edges of terraces where the silicon atoms with two dangling bonds are present. Kink side silicon atoms on (111) surface can be bonded to one hydrogen atom and one –OH group [46], this site being more susceptible to interact with chloroplatinate complexes. Due to the accumulation of (111) terraces, bigger steps are present on the SBSiS with two dangling bonds at step sites. Therefore, it can be supposed that some of them are terminated by one –OH group [21] and that they can interact with chloroplatinate complexes.

Possible interactions of $PtCl_6^{-2}$ with the silicon surface may involve the faces and edges of the octahedron whose dimension are predicted on the basis of the location of maximum electron density in the anion [47]. According to calculations made by Ayala at al. [48], the square planar $PtCl_4^{-2}$ interacts by all four chlorine atoms. These findings are in good agreement with the electrochemical data published by Lau and Hubbard, showing that the $PtCl_4^{-2}$ complex requires more free space on the surface in comparison with $PtCl_6^{-2}$ [44, 45]. Based on current knowledge, it is difficult to discus if $PtCl_4^{-2}$ ions are demanding more space for adsorption on the Si surface.

Despite of geometrical differences between platinum complexes and silicon surface lattice, the attachment of these two components should be possible. Figure 18 presents a sketch of Si(111) surface showing terrace and kink sites with –H and –OH dangling bonds. A possible pathway for the approach of the $PtCl_6^{-2}$ ion to the hydrogen atom of –OH is indicated.

The energetic situation at the *n*-Si surface–electrolyte interface is shown in Fig. 19a. In this figure, it can be seen that the redox potential of $PtCl_6^{-2}$/Pt is located slightly below the valence band of the semiconductor. The first peak at −0.38 V vs. SCE observed on the *I–V* curve in Fig. 4 appears at a potential more positive than the flat band potential (−0.457 V vs. SCE) [49], which means that the surface is under depletion conditions. In equilibrium, in a potential range where the Fermi level of the semiconductor approaches the redox potential of the electrolyte, a strong inversion condition is expected. At −0.8 V vs. SCE, at the potential for the platinum deposition peak in Fig. 4, the semiconductor is in an accumulation situation (Fig. 19b). Possible processes that take place on the silicon surface at this potential are shown in Fig. 20. Electrons from the conduction band of the semiconductor take part in the process of platinum reduction (upper part of Fig. 20). Due to the proximity of the redox potential to the valence band edge of the semiconductor, a charge transfer by hole injection is feasible. This, in turn, may lead to silicon oxidation (formation of silicon dioxide). This process occurs simultaneously with the reduction of Pt species (lower part of Fig. 20). It is also possible that the process takes place by surface states, not marked on the diagram, that are even more accessible in accumulation situation as where the Fermi level of the semiconductor is shifted upwards.

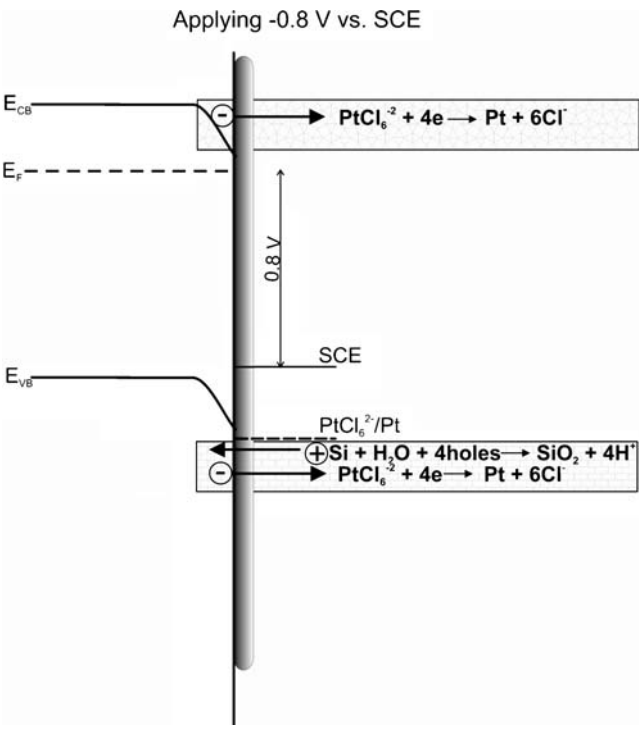

Fig. 20 Energy band diagram for the *n*-Si surface immersed in the platinum electrodeposition solution when the potential −0.8 V vs. SCE is applied, showing possible charge transfers with subsequent reactions

AMV RT deposition on step-bunched Si(111)

AMV RT molecules deposited on the SBSiS can be seen in the TM-AFM images of Fig. 21a. The enlarged image of the biomolecule shows the two heterodimer subunits one on top of each other. From the cross sections shown in Fig. 21b, the immobilization sites of the biomolecules can bee seen. They are mostly localized on the step edges of the terraces of SBSiS. The biomolecules have a diameter of 30 to 40 nm and a height between 2 and 3 nm, which is in good agreement with previously performed STM experiments [29].

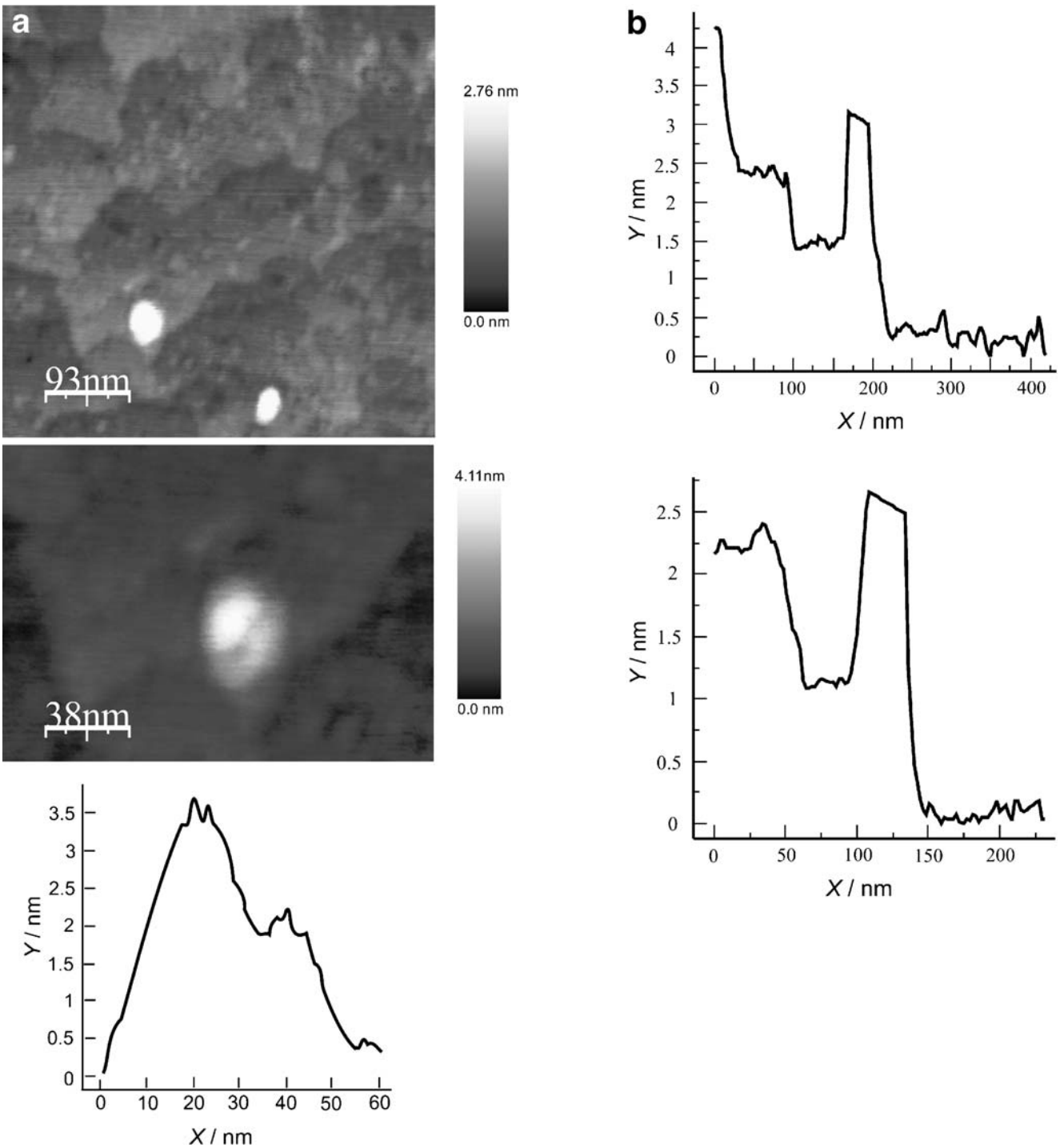

Fig. 21 **a** TM-AFM image of the SBSiS with deposited AMV RT. The picture presents the zoom of the biomolecules with the cross section. **b** Cross sections of the TM-AFM image showing the positions of AMV RT on SBSiS

The biomolecules contain a very thin buffering layer film of biowater [50], which allows for reliable imaging. This fact could be also addressed to the use of tapping mode where the cantilever lightly taps the surface of the sample at the bottom of each oscillation. The short contact between tip and sample allows to get very good resolution due to the short range of van der Waals repulsion between tip and biomolecule.

The biomolecule adsorption on surfaces can be driven by the so-called Derjaguin–Landau–Verwey–Overbeek (DLVO) and non-DLVO forces [51]. The first one includes van der Waals interactions and electrostatic forces, whereas the second one involves steric hydration forces and mechanical forces.

Chemical bonding between the SBSiS and adsorbed biological molecules is less probable. The covalent immobilization of biomolecules requires a surface modification by attachment of special groups that are able to bond proteins [52]. The simple precipitation of buffer solution containing the biomolecules on the silicon surface results in small probability for covalent bonding.

Due to their short-range nature, van der Waals interactions seems to play a remarkable role in the discussed system. These forces can be responsible for the interaction after biomolecules approach the surface. The site-specific adsorption, however, seems to be driven mainly by long-range electrostatic interactions between AMV RT and the negatively charged steps of SBSiS. The dialysis process of the AMV RT performed at pH below the IP of RT (pH_{IP}= 8.3) makes the overall charge on the biomolecule positive so that it can interact electrostatically with the negatively charged steps on the silicon surface. In addition, the topography of the SBSiS, where the steps establish a spatial barrier for the deposited particles, can have some effect on the final position of the deposits.

Platinum and AMV RT on the step-bunched silicon surface

Deposition on SBSiS seems to present some similarities in the spatial selectivity for different materials such as platinum and RT. A clear connection between the surfaces topography and the position of the deposits can be seen in Figs. 13, 14, and 20. The localization of the deposited particles suggests that the deposition of platinum as well as RT is favored at the edges of the terraces. In the case of platinum, the nucleation sites seem to have final localization on step edges, but whether metal dots start to grow at this position cannot be confirmed. The site-specific biomolecule adsorption can be connected with the existence of an inhomogeneous accumulation layer at the step edges of the SBSiS. In the case of platinum, small dots of metal are attached to tips of the zigzag structures also on the H-terminated silicon surface (Fig. 13) at flat band conditions. This suggests that not only the electronic surface properties influences the localization of deposits but also other factors such as topography and surface composition have some contribution. Certainly, there is an influence of the special properties of the SBSiS on the electrodeposition process. This is evident in both the smaller-sized deposited particles localized along the step edges and the lesser amount of silicon oxide found on the surface in comparison with the H-terminated sample. Unfortunately, on this stage of knowledge, it is difficult to explain this phenomenon.

After the deposition, attachment of platinum and AMV RT to the surface by chemical bonds is less probable. In this case, the van der Waals interactions seem to play the main role.

Summary and outlook

The chemical and electrochemical preparation of high-quality nanostructured silicon surfaces such as H-terminated and step-bunched surfaces was described. The chemical, electronic, and topographical properties of the surfaces were investigated with SRPES, HREELS, and TM-AFM. On well-defined surfaces, the site-specific adsorption was performed. For deposition, platinum by electrochemical reduction of chloroplatinate complexes and dialyzed AMV RT molecules in buffer solution were used. The deposition of platinum was performed on the H-terminated reference silicon surface as well as on SBSiS. It was advocated that due to the close position of the semiconductor valence band and electrolyte redox potential as well as the presence of surface states, the silicon oxide is synthesized during the described experiment. The AMV RT was deposited on SBSiS only. Deposited particles were found attached preferentially at the step edges on the SBSiS. This confirms the influence of a localized accumulation layer at SBSiS on depositing particles, especially AMV RT. Certainly, factors such as van der Waals interactions and steric properties have to be also taken into account.

Acknowledgement The authors would like to acknowledge H.J. Lewerenz, H. Jungblut, A. Munoz, and S. Fiechter for the discussions and support. The Bessy team composed of M. Kanis, M. Lublow, and Th. Stempel; the HREELS team composed of K. Jacobi, P. Geng, Th. Wilhelm, and M. Kanis; the KPM team composed of S. Sadewasser and F. Streicher; and the Biological team composed of S. A. Campbell, J.R. Smith and D. Mernagh are gratefully acknowledged.

References

1. Gonzalez-Garcia J, Iniesta J, Exposito E, Garcia-Garcia V, Montiel V, Aldas A (1999) Thin Solid Films 352:49. doi:10.1016/S0040-6090(99)00331-4

2. Prod'homme P, Maroun F, Cortes R, Allongue P, Hamrle J, Ferre J et al (2007) J Magn Magn Mater 315:26. doi:10.1016/j.jmmm.2007.02.199
3. Jenq SN, Wan CC, Wang YY, Li HW, Liu PT, Chen JH (2006) Electrochem Solid-State Lett 9(10):C167 doi:10.1149/1.2236375
4. Deep Chopra H, Hua SZ (2002) Phys Rev B 66:020403. doi:10.1103/PhysRevB.66.020403
5. Rastei MV, Colis S, Bucher JP (2006) Chem Phys Lett 41:7217
6. Wang R, Hu YX (2003) J Biomed Mater Res 67A(1):270. doi:10.1002/jbm.a.10114
7. Tofail SAM (2006) Proceeding of the Symposium on Photonics Technologies for 7th Framework Program, Wroclaw
8. Baszkin A, Norde W (2000) Physical chemistry of biological interfaces. Marcel Dekker, New York
9. Zoval JV, Lee J, Gorer S, Penner RM (1998) J Phys Chem B 102:1166. doi:10.1021/jp9731967
10. Parker MC, Patel N, Davies MC, Roberts CJ, Tendler SJB, Williams PM (1996) Protein Sci 52:329
11. Yoshinobu T, Suzuki J, Kurooka H, Moon WC, Iwasaki H (2003) Electrochim Acta 48:3131. doi:10.1016/S0013-4686(03)00342-6
12. Skorupska K, Aggour M, Kanis M, Lublow M, Jungblut H, Lewerenz HJ (2007) ECS Trans 2:1. doi:10.1149/1.2408985
13. Aggour M, Skorupska K, Stempel Pereira T, Jungblut H, Grzana J, Lewerenz HJ (2007) J Electrochem Soc 154(9):H794. doi:10.1149/1.2756366
14. Hodneland CD, Lee YS, Min DH, Mrksich M (2002) Proc Natl Acad Sci U S A 99(8):5048. doi:10.1073/pnas.072685299
15. Shyakhtenko LS, Jaffrey AA, Weimer J, Hawn DD, Lyubchenko YL (1999) Biophys J 77:568
16. Härtl A, Schmich E, Garrido JA, Hernando J, Catharino SCR, Walter S et al (2004) Nat Matters 37:38
17. Heron W, Rebien M, Angermann H, Röseler A (2002) Appl Surf Sci 202:199. doi:10.1016/S0169-4332(02)00923-6
18. Morrison SR (1980) Electrochemistry at semiconductor and oxidized metal electrodes. Plenum, New York, pp 65–72
19. Garcia SP, Bao H, Hines MA (2004) Phys Rev Lett 93 (16):166102. doi:10.1103/PhysRevLett.93.166102
20. Skorupska K, Lublow M, Kanis M, Jungblut H, Lewernz HJ (2005) Appl Phys Lett 87:262101. doi:10.1063/1.2150267
21. Skorupska K, Lublow M, Kanis M, Jungblut H, Lewerenz HJ (2005) Electrochem Commun 7:1077. doi:10.1016/j.elecom.2005.07.012
22. Skorupska K, Smith JR, Campbell SA, Jungblut H, Lewerenz HJ (2007) ECS Trans 2:63. doi:10.1149/1.2409009
23. Wang J, Smerdon SJ, Jäger J, Kohlstaedt LA, Rice PA, Friedman JM (1994) Proc Natl Acad Sci U S A 91:7242. doi:10.1073/pnas.91.15.7242
24. Jacobo-Molina A, Ding J, Nanni RG, Clark AD, Lu X, Tantilio C et al (1993) Proc Natl Acad Sci U S A 91:6320. doi:10.1073/pnas.90.13.6320
25. Szilvay A, Stern B, Blichenberg A, Helland DE (2000) FEBS Lett 484:43. doi:10.1016/S0014-5793(00)02113-X
26. Darst SA, Kubalek EW, Kornberg RD (1989) Nature 340:730. doi:10.1038/340730a0
27. Bressanelli S, Tomei L, Roussel A, Incitti I, Vitale RL, Mathieu M et al (1999) Proc Natl Acad Sci U S A 96(23):13034. doi:10.1073/pnas.96.23.13034
28. Joyce CM, Steitz TA (1994) Annu Rev Biochem 63:777. doi:10.1146/annurev.bi.63.070194.004021
29. Campbell SA, Smith JR, Jungblut H, Lewerenz HJ (2007) J Electroanal Chem 599:313. doi:10.1016/j.jelechem.2006.05.035
30. Jacobi K, Gruyters M, Geng P, Bitzer T, Aggour M, Rauscher S et al (1995) Phys Rev B 51(8):5437. doi:10.1103/PhysRevB.51.5437
31. Dumas P, Chabal YJ (1991) Chem Phys Lett 182(6):537. doi:10.1016/0009-2614(91)80309-L
32. Skorupska K, Streicher F, Aggour M, Sadewasser S, Kanis M, Baohui X et al (2007) 211th ECS Meeting, Abstract #624, The Electrochemical Society
33. Lewerenz HJ, Jungblut H, Rauscher S (2000) Electrochim Acta 45:4627. doi:10.1016/S0013-4686(00)00613-7
34. Himpsel FJ, McFeely FR, Taleb-Ibrahimi A, Yarmoff JA (1988) Phys Rev B 38(9):6084. doi:10.1103/PhysRevB.38.6084
35. Hüfner S, Wertheim GK (1975) Phys Rev B 11(2):678 doi:10.1103/PhysRevB.11.678
36. Borisenko VE, Hesketh PJ (1997) Microdevices, physic and fabrication technology: rapid thermal processing of semiconductors. Plenum, New York, p 167
37. Lu G, Zangari G (2005) J Phys Chem B 109:7998
38. Gollas B, Elliott JM, Bartlett PN (2000) Electrochim Acta 45:3711. doi:10.1016/S0013-4686(00)00464-3
39. Greef R, Peat R, Peter LM, Pletcher D, Robinson J (1985) Instrumental methods in electrochemistry. Horwood, Chichester, p 76
40. Sawaguchi T, Yamacha T, Okinaka Y (1995) J Phys Chem 99:14149. doi:10.1021/j100038a056
41. Ge M, Zhong B, Klemperer WG, Gewirth AA (1996) J Am Chem Soc 118:5812. doi:10.1021/ja960498y
42. Uosaki K, Ye S, Oda Y, Haba T, Hamada K (1997) Langmuir 13:594. doi:10.1021/la960728m
43. Uosaki K, Ye S, Naohara H, Oda Y, Haba T, Kondo T (1997) J Phys Chem B 101:7566. doi:10.1021/jp9717406
44. Lau ALY, Hubbard AT (1971) J Electroanal Chem 33:77. doi:10.1016/S0022-0728(71)80210-3
45. Lau ALY, Hubbard AT (1970) J Electroanal Chem 24:237. doi:10.1016/S0022-0728(70)80148-6
46. Lewerenz HJ, Aggour M, Murrell C, Kanis M, Jungblut H, Jakubowicz J et al (2003) J Electrochem Soc 150(3):E185. doi:10.1149/1.1542900
47. Naidoo KJ, Lopis AS, Westa AN, Robinson DJ, Koch KR (2003) J Am Chem Soc 125:13330. doi:10.1021/ja035326x
48. Ayala R, Marcos ES, Diaz-Moreno S, Sole VA, Munoz-Paez A (2001) J Phys Chem B 105:7588. doi:10.1021/jp010326+
49. Munoz AG, Lewerenz HJ (2008) J Electrochem Soc 155:D527
50. Kumar S, Peon J, Zewail AH (2002) Proc Natl Acad Sci U S A 99 (4):1763. doi:10.1073/pnas.042683699
51. Malmsten M (ed) (1998) Biopolimers at the surfaces. Marcel Dekker, New York
52. Bhushan B, Tokachichu DR, Keener MT, Lee SC (2005) Acta Biomater 1:327. doi:10.1016/j.actbio.2005.01.002